

# The Tipping Point: how tip asymptotics can enhance numerical modeling of hydraulic fracture evolution

A. PEIRCE

*Department of Mathematics, University of British Columbia, Vancouver, British Columbia, V6T 1Z2, Canada.*

*(Received 21 March 2023)*

Developing numerical schemes to model the evolution of hydraulic fractures is particularly challenging due to the degenerate, hypersingular nature of the coupled integro-partial differential equations along with a singular free boundary, whose velocity is typically only defined in terms of a distinguished limit. This chapter describes how the tip asymptotic behavior can be exploited to locate the fracture free boundary as well as capture the multiscale effects relevant at the computational scale in a weak form. We illustrate the technique in the context of the Displacement Discontinuity (DD) formulation continuum governing equations on a structured mesh. Numerical examples are provided to illustrate the performance of the numerical scheme.

Key words: Hydraulic Fracture , Free Boundary, Multi-Scale tip asymptotics, Level Set Methods, DD Method.

## 1 Introduction

Hydraulic fractures (HF) are a class of brittle fractures that propagate in pre-stressed solid media due to the injection of a viscous fluid. On a geological scale, HF occur as kilometers-long vertical dikes that bring magma from deep underground chambers to the earth’s surface [39]. Industrial applications of HF include: accelerating the waste remediation process, waste disposal, or preconditioning in rock mining [41]. One of the most common industrial applications is reservoir stimulation to enhance the recovery of hydrocarbons to create permeable pathways [14].

Inspired by the seminal 1987 paper by Spense and Sharp [38] and the 1994 discovery of the so-called “SCR viscous asymptote” [7], the beginning of this millennium heralded intense research into the propagation of HF in the special case of plane strain. See [8] for an excellent review of this corpus of research, which established the pivotal role of the asymptotic behavior of the solution in the vicinity of the fracture tip and the complex multiscale structure of the solution in which two or more physical processes compete at multiple length and time scales.

However, progress on incorporating this multiscale structure into numerical models has lagged behind these developments. Despite significant progress made since the first algorithms were developed in the 1970’s [5], many 3D HF algorithms still use propagation criteria based on the LEFM of dry cracks (see the 2007 review of numerical models [2]). This lag in development is due to the intrinsic complexity of the coupled HF equations, which involve a degenerate hypersingular integro-delay-PDE along with a singular free boundary problem. It was not clear how to develop numerical models of HF in 3D elastic media with arbitrarily shaped boundaries able to capture the multiscale structure without prohibitively expensive and complex re-meshing. In this chapter we describe how the tip asymptotic behavior is an essential tool in the construction of numerical schemes that can locate the unknown fracture boundary and capture the multiscale behavior on a coarse mesh [31, 33, 13, 34].

In section 2, we state the governing equations for the elastic medium, fluid flow, boundary conditions, and tip asymptotics; in section 3, we discuss discretization of the DD equations, solving the coupled equations, and locating

the free boundary using the implicit level set method; in section 4 we provide numerical examples; in section 5 we provide concluding remarks.

## 2 Mathematical Model

### 2.1 Assumptions

The equations governing the propagation of a HF in a reservoir have to account for the dominant physical processes taking place during the treatment, namely: deformation of the rock; creation of new fracture surfaces; flow of fracturing fluid in the crack; leak-off of fracturing fluid into the reservoir. We consider the governing equations for hydraulic fracture propagation that involve continuum descriptions of fracture in the solid medium and fluid flow within the fracture. For the solid medium we choose to discuss the displacement discontinuity (DD) boundary integral formulation and assume: (i) that the rock is homogeneous, linear elastic, brittle, permeable and of infinite extent whose stiffness is characterized by the Young's modulus  $E$  and Poisson's ratio  $\nu$ , while the energy required to break the rock is represented by the fracture toughness  $K_{Ic}$ ; (ii) the fracturing fluid is incompressible and Newtonian with a dynamic viscosity  $\mu_f$ ; (iii) Carter's leak-off [4] is used to model loss of fluid to the reservoir and characterized by the coefficient  $C_L$ ; (iv) the fracture evolves in a plane orthogonal to the minimum *in situ* confining stress field  $\sigma_0(x, y)$ ; (v) high confinement conditions prevail so the fluid front rapidly coalesces with the crack front [16].

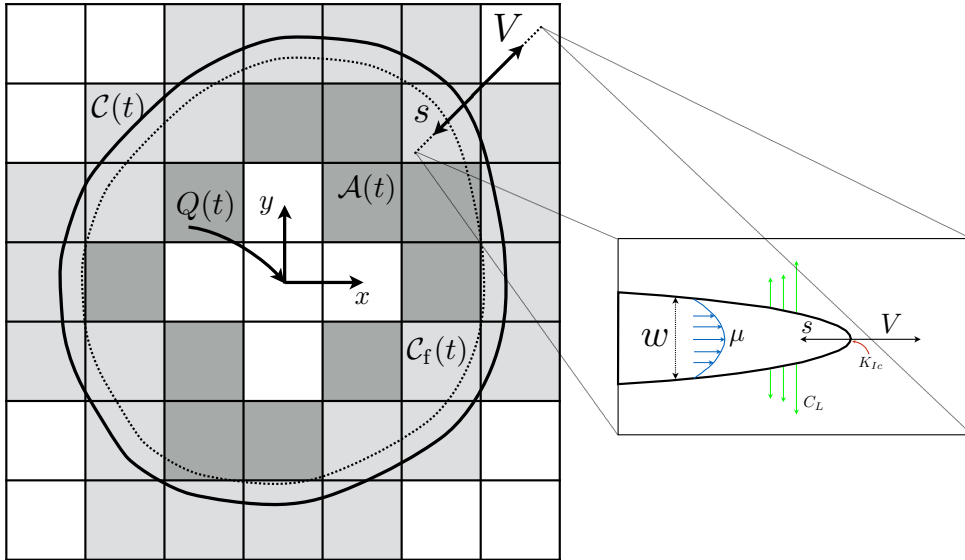


FIGURE 1. The planar fracture footprint  $\mathcal{A}(t)$  inscribed within curve  $\mathcal{C}(t)$  moving with normal velocity  $V$  and driven by the fluid contained within the dashed curve  $\mathcal{C}_f(t)$ . The  $xy$  coordinate system is centered on the point source.

The solution of the hydraulic fracture problem involves determining the fracture aperture  $w(x, y, t)$ , the fluid pressure  $p_f(x, y, t)$ , the fluid flux  $\mathbf{q}(x, y, t)$ , and the position of the front  $\mathcal{C}(t)$ , where  $t$  denotes the time and  $x, y$  are coordinates referenced to the injection point (see figure 1(a)). The solution depends on the injection rate  $Q(t)$ , the far-field compressive stress perpendicular to the fracture plane  $\sigma_0(x, y)$  (a known function of position), and the four material parameters  $\mu'$ ,  $C'$ ,  $E'$ , and  $K'$  defined as

$$\mu' = 12\mu_f, \quad C' = 2C_L, \quad E' = \frac{E}{1 - \nu^2}, \quad K' = 4 \left( \frac{2}{\pi} \right)^{1/2} K_{Ic}. \quad (2.1)$$

Here  $E'$  is the plane strain modulus, and the alternate viscosity  $\mu'$ , leak-off  $C'$ , and toughness  $K'$  are introduced to keep the equations uncluttered by numerical factors.

## 2.2 Governing Equations

### 2.2.1 Elasticity

In view of the rock homogeneity and linear elasticity assumptions, the elasticity equation that relates the fracture aperture  $w$  to the compressive stress field along the crack (which is related to the fluid pressure  $p_f$ ) can be condensed into a single hypersingular integral equation [6]

$$p_f(x, y, t) = \sigma^h(y) - \frac{E'}{8\pi} \int_{\mathcal{A}(t)} \frac{w(x', y', t) dx' dy'}{[(x' - x)^2 + (y' - y)^2]^{3/2}}, \quad (2.2)$$

where  $\mathcal{A}(t)$  denotes the fracture footprint, i.e. the area enclosed by the crack front  $\mathcal{C}(t)$  (see Fig. 1) and  $\sigma^h(y)$  is the prescribed *in-situ* geological stress field.

### 2.2.2 Fluid transport

By combining Poiseuille's law  $\mathbf{q} = -\frac{w^3}{\mu'} \nabla p_f$  and the continuity equation  $\frac{\partial w}{\partial t} + \nabla \cdot \mathbf{q} + \frac{C'H(t-t_0(x,y))}{\sqrt{t-t_0(x,y)}} = Q(t)\delta(x, y)$ , we obtain the Reynolds lubrication equation

$$\frac{\partial w}{\partial t} = \frac{1}{\mu'} \nabla \cdot (w^3 \nabla p_f) - \frac{C'H(t-t_0(x,y))}{\sqrt{t-t_0(x,y)}} + Q(t)\delta(x, y). \quad (2.3)$$

where the trigger-time  $t_0(x, y)$  represents the time at which the unknown fracture front passes the point  $(x, y)$  constitutes a history term  $t_0(x, t)$ , which is not known *a priori* so that (2.3) is a delay partial differential equation.

### 2.2.3 Boundary and propagation conditions

For this nonlinear problem there exist multiple equilibrating and volume-conserving width and pressure fields, so imposing the appropriate boundary and propagation conditions is the key to selecting the desired global solution [9].

#### Finite lag between fluid and fracture fronts

When the fluid front  $\mathcal{C}_f(t)$  is distinct from and entirely contained within the fracture front  $\mathcal{C}(t)$  there is a finite lag between the two fronts the boundary and propagation conditions are:

$$p_f(\mathbf{x}, t) = 0 \text{ and } \mathbf{V}_f(\mathbf{x}, t) = \mathbf{q}(\mathbf{x}, t)/w(\mathbf{x}, t) \text{ for } \mathbf{x} \in \mathcal{C}_f(t), \quad (2.4)$$

$$w(\mathbf{x}, t) = 0 \text{ and } K_I(\mathbf{x}, t) = K_{Ic} \text{ for } \mathbf{x} \in \mathcal{C}(t). \quad (2.5)$$

In each of (2.4)-(2.5) the first conditions prescribe boundary conditions on the fluid pressure and width fields, while the second conditions in (2.4)-(2.5) respectively provide the Stefan condition for the moving fluid front  $\mathcal{C}_f(t)$  and the propagation condition that the stress intensity factor match the fracture toughness at all points of  $\mathcal{C}(t)$ .

#### Coalescent fluid and fracture fronts

For most HF treatments the confining stress  $\sigma_0$  is large compared to the characteristic driving stress  $\mu'VE'^2/K'^2$  causing the lag to vanish rapidly [16]. Rather than resolve this vanishingly small lag with a fine mesh it is more efficient to establish the appropriate boundary conditions for the limit  $\mathcal{C}_f(t) \rightarrow \mathcal{C}(t)$  [9]. For an impermeable medium, as  $\mathbf{x} \in \mathcal{C}_f \rightarrow \mathcal{C}$  the corresponding width  $w(\mathbf{x}, t) \rightarrow 0$ , thus from (2.4(b)) in order that  $|\mathbf{V}_f|$  remain finite it follows that

$\mathbf{q}(\mathbf{x}, t) \rightarrow 0$ . The limit for a permeable medium is more subtle [9] but yields the same result, so (2.4)-(2.5) reduce to

$$w(\mathbf{x}, t) = 0, \quad K_I(\mathbf{x}, t) = K_{Ic}, \quad \text{and } \mathbf{q}(\mathbf{x}, t) = 0 \text{ for } \mathbf{x} \in \mathcal{C}(t). \quad (2.6)$$

From the propagation condition  $K_I = K_{Ic}$  and LEFM it follows [35] that

$$w \sim \frac{K'}{E'} s^{1/2}, \quad (2.7)$$

where  $s$  (see figure 1(a)) denotes the distance from the crack front  $\mathcal{C}(t)$ . Since the front velocity  $\mathbf{V}$  for an impermeable medium is equal to the average fluid velocity as  $s \rightarrow 0$  it follows that

$$\mathbf{V} = \frac{1}{\mu'} \lim_{s \rightarrow 0} w^2 \nabla p_f, \quad (2.8)$$

which shows that  $\mathbf{V}$  is the limit of an indeterminate form, which is difficult to evaluate numerically. For a permeable medium, in the region of dominant leak-off the average fluid velocity tends to infinity as  $s \rightarrow 0$ , and the crack front velocity needs to be determined by detailed asymptotic analysis [9]. Thus front location algorithms [37] based on knowing the front velocity  $\mathbf{V}$  explicitly, cannot be applied directly to this singular free boundary problem.

#### 2.2.4 Tip asymptotics, vertex solutions, and generalized asymptotes

A propagating HF with zero lag is governed by two competing dissipative processes: one associated with viscous energy losses and the other with the energy expended in breaking the rock, which is characterized by the fracture toughness; and two competing fluid-balance components: fluid storage in the fracture and storage in the surrounding rock - associated with leak-off. Limiting regimes can be identified in which just one of the dissipative processes and one of the storage mechanisms is dominant. Associated with each of these limiting regimes are so-called vertex solutions with reference to vertices of a multi-process phase space within which the dissipative and storage mechanisms compete. For example, for the storage-viscosity regime known as the  $m$ -vertex, leak-off is negligible compared to the fluid stored in the fracture and the energy expended breaking the rock is negligible compared to viscous dissipation, so that  $K' \approx 0 \approx C'$ . A HF having radial symmetry and for which  $K' \neq 0 \neq C'$  will change its regime of propagation over time during which multiple length and time scales are important (see [31, 8] for further details). The key tool to characterize this multiprocess multiscale environment is an analysis of the tip asymptotics and the so-called semi-infinite fracture problem.

##### *Tip asymptotics and semi-infinite crack problem*

Provided the fracture front  $\mathcal{C}$  is sufficiently smooth that a finite radius of curvature can be defined at each point along its perimeter and assuming a homogeneous elastic medium it can be shown [31] that the governing equations (2.2), (2.3), and (2.7) for the aperture  $w$  and net pressure  $p$  in the vicinity of the fracture front reduce to those for a semi-infinite fluid-driven fracture steadily propagating in a state of plane-strain at a constant velocity  $V$  and characterized by zero lag (see [16]), namely:

$$\frac{\hat{w}^3}{\mu'} \frac{d\hat{p}}{ds} = V\hat{w} + 2C'V^{1/2}s^{1/2}, \quad \hat{p} = \frac{E'}{4\pi} \int_0^\infty \frac{d\hat{w}}{dz} \frac{dz}{s-z}, \quad \lim_{s \rightarrow 0} \frac{\hat{w}}{s^{1/2}} = \frac{K'}{E'}. \quad (2.9)$$

Here  $s$  represents a coordinate located on the moving tip and pointing toward the interior of the fracture. The consequence of this reduction is profound in that the tip asymptotic solution for a *finite fracture* at any time is given by the solution of the stationary semi-infinite crack in a state of plane strain whose constant tip velocity corresponds to the *current* propagation speed of the finite fracture. The tip solution is thus autonomous. Note that the spatial

variation of the far-field stress can be ignored when viewed at the tip scale, unless the stress field is discontinuous (in which case, the tip solution outlined here is not relevant).

*Vertex solutions*

Assuming the fracture width is given by a power law  $\hat{w} = As^\alpha$  and recognizing that in this case the integral operator (2.9) reduces to a Mellin Transform, it follows [25] that

$$\hat{p} = \frac{E'A\alpha}{4\pi} \int_0^\infty \frac{z^{\alpha-1}}{s-z} dz = \frac{1}{4}E'A\alpha \cot(\pi\alpha)s^{\alpha-1}, \quad 0 < \alpha < 1 \quad (2.10)$$

Thus for this range of values of  $\alpha$  the power law is an eigenfunction of the integral operator in (2.10).

This power law solution pair can be used to identify the three limiting regimes of propagation also known as vertex solutions, namely: the viscosity dominated solution, the leak-off dominated solution, and the toughness dominated solution. Choosing  $\alpha \neq 1/2$  and substituting the power law behavior  $\hat{w} = As^\alpha$  and the corresponding power law behavior for  $\hat{p}$  given by (2.10) into the lubrication equation in (2.9a) we can obtain two different vertex solutions by identifying two distinct dominant balances. Choosing the dominant balance between the term on left side and the first term on the right, we find that  $\alpha = 2/3$  and matching coefficients yields the so-called  $m$ -vertex solution [7]

$$w_m = \beta_m \left( \frac{\mu'V}{E'} \right)^{1/3} s^{2/3}, \quad p_m = O(s^{-1/3}), \quad \beta_m = 2^{1/3}3^{5/6}. \quad (2.11)$$

Choosing a dominant balance between the term on the left and the second term on the right of (2.9a), we obtain that  $\alpha = 5/8$  and matching coefficients we obtain the so-called  $\tilde{m}$ -vertex solution [23]

$$w_{\tilde{m}} = \beta_{\tilde{m}} \left( \frac{4\mu'^2 C'^2 V}{E'^2} \right)^{1/8} s^{5/8}, \quad p_{\tilde{m}} = O(s^{-3/8}), \quad \beta_{\tilde{m}} = 4/(15(\sqrt{2}-1))^{1/4}. \quad (2.12)$$

Finally, if  $\alpha = 1/2$  then the toughness asymptote (2.7) is the so-called  $k$ -vertex solution  $w_k$  and matching the term on the left of (2.9a) with the first term on the right we find that  $p_k = O(\log(s))$ .

*Generalized asymptotes*

From the vertex solutions described above we see that for  $s \ll 1$  there is a hierarchy of powers

$$s^{1/2} \gg s^{5/8} \gg s^{2/3} \quad (2.13)$$

that establishes the region moving away from the fracture tip that will be occupied by the different solutions. For example closest to the tip the toughness solution (provided  $K' > 0$ ) will always be dominant. Then provided  $C' \gg 0$ , as one moves further from the tip, the solution will transition to the leak-off asymptote characterized by the 5/8 power law. The length scale at which this transition occurs is determined by the relative magnitudes of the coefficients of the two solutions. Finally, the leak-off solution will transition to the viscous solution characterized by the 2/3 power which prevails farthest from the tip. Thus we can see that there are multiple physical processes possible that can be active at vastly different length scales. If only two of these processes are present then the same ranking in (2.13) determines the regions occupied by the two processes relative to the tip.

Garagash [15] was the first to consider a two process solution involving the transition from the toughness to the viscous dominated regimes ( $C' = 0$ ) by solving the semi-infinite crack problem (2.9) with the boundary condition at infinity  $\hat{w} \xrightarrow{s \rightarrow \infty} w_m(s)$ . The numerical solution to this connection problem (shown in figure 4 (b)) involves the generalized asymptote  $\hat{\Omega}$  in terms of which the asymptotic solution can be expressed in the form:

$$w_{mk} = \frac{K'^4}{E'^3 \mu' V} \hat{\Omega}(s/\ell_{mk}), \quad \ell_{mk} = \frac{K'^6}{E'^4 \mu'^2 V^2}, \quad (2.14)$$

where  $\ell_{mk}$  is the transition length scale. The  $m$  and  $k$  vertex solutions as well as the  $m - k$  transition solution have all been observed experimentally for penny-shaped fractures [3, 8].

The corresponding viscous to leak-off transition ( $K' = 0$ ) involving the transition length scale  $\ell_{m\tilde{m}} = \frac{2^6 C'^6 E'^2}{\mu'^2 V^5}$  has been considered by [1]. Having established the two-process ‘‘edge solutions’’ Garagash *et al* [17] have provided the numerical solution for the generalized tip asymptotics for an HF in which all three processes are active ( $K' > 0$ ,  $\mu' > 0$ ,  $C' > 0$ ). This generalized asymptote involves multiple length scales, which are characterized by the dimensionless parameter  $\chi = \left(\frac{\ell_{m\tilde{m}}}{\ell_{mk}}\right)^{1/6} = \frac{2C'E'}{K'V^{1/2}}$ . Recently [11] a simpler non-singular formulation of the hypersingular integral equation (2.9) has made it possible to solve the multiscale problem using standard numerical techniques and yields an approximate formulation in terms of a separable first order ordinary differential equation (ODE). The closed form solution of this ODE yields not only all the vertex solutions but also the following approximate solution [11, 13] for  $\tilde{w} := \frac{E'w}{K's^{1/2}}$  given  $\tilde{s} = \left(\frac{s}{\ell_{mk}}\right)^{1/2}$  defined implicitly in terms of a given function  $g_\delta$

$$\frac{\tilde{s}}{\tilde{w}^3} = g_\delta \left( \frac{1}{\tilde{w}}, \frac{\chi}{\tilde{w}} \right), \quad (2.15)$$

which is able to capture the complete multiscale solution within a fraction of a percent. A contour map of  $\tilde{w}$  as a function of  $\tilde{s}$  and  $\chi$  is shown in figure 3, in which the transitions between the  $m$ ,  $k$ , and  $\tilde{m}$  can be clearly observed. This generalized asymptote has been used to model 3-process multiscale planar [13] and multi-planar [12] hydraulic fractures.

### 3 Discretization, Coupled Equations, and the multiscale ILSA scheme to locate the free boundary

In this section we briefly describe the discretization of the DD equations on a structured rectangular mesh. Since the resulting coupled evolution equations are extremely stiff (for which explicit schemes require time step restrictions  $\Delta t \leq O(\Delta x^3)$  [29, 2]) the L-stable backward Euler implicit time stepping is often used to evolve the solution. Hence we also describe iterative schemes and preconditioners that have been developed to solve the fully-coupled equations that need to be solved at each time step. Having established the importance of the tip asymptotic behavior in governing the propagation of HF, we discuss specialized numerical schemes that have been developed to locate the free boundary and to accommodate this multiple length scale behavior that can span 5-20 decades without having to resort to mesh refinement. In a recent comparative study [22] this class of schemes was shown to provide accurate solutions on a relatively coarse fixed structured mesh.

#### 3.1 Discretization

##### 3.1.1 Displacement Discontinuity formulation for planar fractures

We assume [31] that the fracture will grow within a rectangular region that has been tessellated into a fixed uniform rectangular mesh  $\cup \Delta \mathcal{A}_{m,n}$  with dimensions  $\Delta x$  and  $\Delta y$  in the two coordinate directions (similar to the fracture shown in figure 1(a)). The fracture footprint  $\mathcal{A}(t)$  is then covered by rectangular elements  $\Delta \mathcal{A}_{m,n}$  such that  $\mathcal{A} \subseteq \cup \Delta \mathcal{A}_{m,n}$ . Constant displacement discontinuity (DD) elements are used for the elasticity computations [6] along with collocation at element centers to yield a fully populated linear system relating the element net pressures  $p$  to the element widths  $w$

$$p = p_t - \sigma_0 = Cw, \quad (3.1)$$

in which, for a homogeneous elastic medium,  $C$  assumes the convolution form

$$C_{k-m,l-n} = -\frac{E'}{8\pi} \left[ \frac{\sqrt{(x_k - x)^2 + (y_l - y)^2}}{(x_k - x)(x_l - x)} \right]_{x=x_m-\Delta x/2, y=y_n-\Delta y/2}^{x=x_m+\Delta x/2, y=y_n+\Delta y/2}. \quad (3.2)$$

Consistent with the constant DD discretization with collocation at element centers, the lubrication equation (2.3) is discretized via the finite volume method to yield a five node finite difference stencil [40, 31] and the Backward Euler scheme to obtain

$$w - w_{t-\Delta t} = \Delta t A(w) p_f + S, \quad (3.3)$$

where  $S$  is a vector of source/sink terms and  $A(w)$  is the difference operator defined by

$$[A(w)p]_{k,l} = \frac{q_{k+\frac{1}{2},l} - q_{k-\frac{1}{2},l}}{\Delta x} + \frac{q_{k,l+\frac{1}{2}} - q_{k,l-\frac{1}{2}}}{\Delta y}, \quad (3.4)$$

and  $q_{k\pm\frac{1}{2},l}$  are the fluxes along the vertical edges of the element defined as  $q_{k\pm\frac{1}{2},l} = \pm w_{k\pm\frac{1}{2},l}^3 \left( \frac{p_{k\pm\frac{1}{2},l} - p_{k,l}}{\Delta x} \right)$ , where  $w_{k\pm\frac{1}{2},l}$  are the corresponding edge widths defined by  $w_{k\pm\frac{1}{2},l} = \left( \frac{w_{k\pm\frac{1}{2},l} + w_{k,l}}{2} \right)$ . The fluxes and widths along the horizontal edges of the element are defined analogously. Zero flux boundary conditions are implemented in tip elements by removing those terms associated with the element faces having zero boundary fluxes from the difference operator.

Solving the coupled equations (3.1) and (3.3) for  $p_f$  and  $w$  as primary variables requires the inversion of the operator  $A(w)$ , which is rank deficient owing to the Neumann boundary condition on  $p_f$  due to the zero flux boundary condition (2.6c) that holds in the zero lag case. In order to ensure a solution exists in this case it is necessary to impose the solvability condition

$$\int_{\mathcal{A}} (w - w_{t-\Delta t}) dx dy + \Delta \mathcal{L} = Q_0 \Delta t, \quad (3.5)$$

where  $\Delta \mathcal{L}$  is the volume leaked from the fracture over the current time step and (3.5) is obtained by integrating (2.3) in space over the region  $\mathcal{A}$  and in time over  $[t, t + \Delta t]$ , using the divergence theorem, and imposing the zero flux boundary condition (2.6c). To avoid the complexity of having to impose the solvability condition (3.5) we use (3.1) to eliminate  $p_f$  from (3.3) to obtain the following evolution equation for the width  $w$  at time  $t$

$$w = w_{t-\Delta t} + \Delta t A(w)(Cw + \sigma_0) + S. \quad (3.6)$$

Once the width has been determined, the corresponding net and fluid pressures can be obtained directly from (3.1).

This coupled system of nonlinear equations is typically solved by Picard, Fixed-Point, or Newton iterative methods or combinations thereof [34]. The large system of dense linear equations that need to be solved during each of these nonlinear iterations are also typically solved iteratively, which facilitate acceleration methods such as: the FFT [27] and Fast Multipole Method [28] to perform  $C$ -matrix vector products; and preconditioners that significantly reduce the number of linear iterations based on multigrid [29] or Incomplete LU factorizations of localized Jacobian matrices [30].

### 3.2 Locating the free boundary using the implicit level set algorithm (ILSA)

Since there are an infinite number of volume preserving-equilibrating pairs  $(w, p_f)$  that are solutions to the nonlinear equations (3.1) and (3.3), each associated with a slightly different footprint  $\mathcal{A}$ , it is important to select the correct

solution by determining the appropriate fracture boundary  $\mathcal{C}$ . Due to the singular free boundary problem characteristic of HF propagating with zero lag, the local fluid velocity in the vicinity of the tip, which requires the numerical evaluation of a distinguished limit, cannot be used to locate the free boundary  $\mathcal{C}$ .

Indeed, the algorithm to locate the free boundary has to incorporate the singular tip asymptotics discussed in section 2.2.4. We now describe the Implicit Level Set Algorithm (ILSA) [31, 33, 13] that was developed to use the tip asymptotics to locate the fracture free boundary. It is notionally convenient to separate the DD elements representing the fracture into two sets, namely: the tip elements  $\mathcal{A}^t$  and the channel elements  $\mathcal{A}^c$ . The tip elements are the partially filled elements colored by light shading in figure 1, while the channel elements comprise those elements surrounded by the tip elements that are completely filled with fluid. We also identify the ribbon of channel elements  $\partial\mathcal{A}^c$  on the boundary of the channel region  $\mathcal{A}^c$  that share at least one side with a tip element (see the dark shaded elements in figure 1(a)), which we refer to as survey elements.

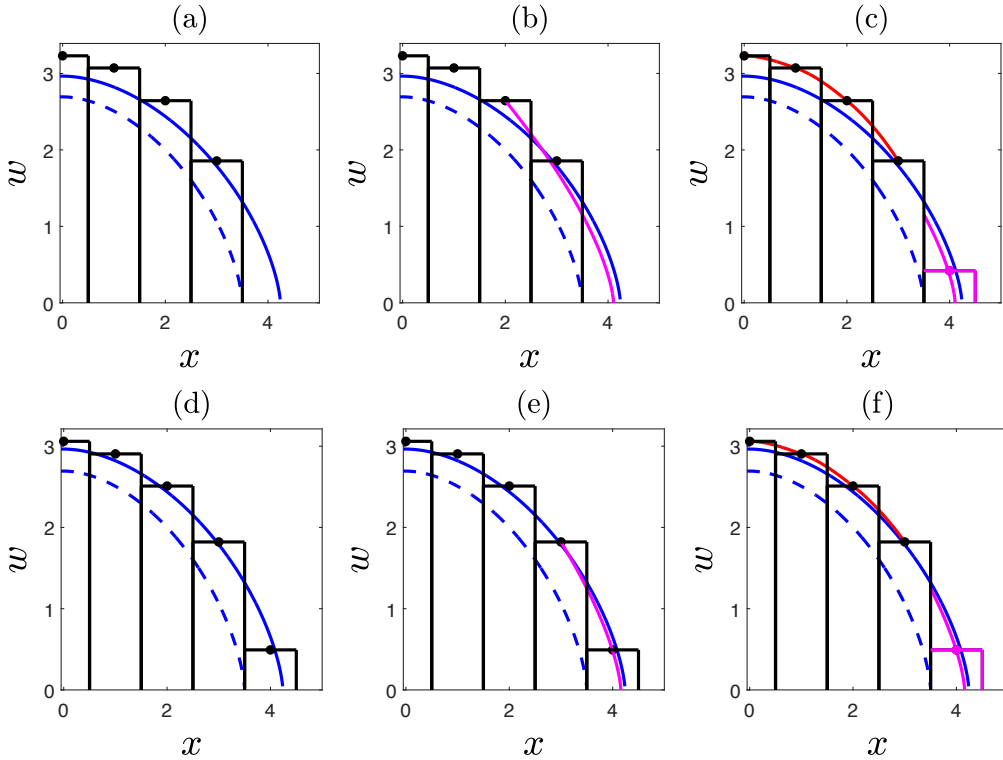


FIGURE 2. Steps used by the ILSA scheme to locate the fracture free boundary using the tip asymptote

### Steps in the ILSA procedure:

The steps in the ILSA algorithm are illustrated in figure 2 in which width cross sections  $w(x, 0, t)$  are plotted. The blue curves represent the exact width (dashed at time step  $t - \Delta t$  and solid at time step  $t$ ). The black rectangles represent the piecewise constant DD approximations to the crack width. The first row of sub-figures represents the procedure used by the ILSA scheme in the first front iteration, which starts with the injection of a volume of fluid  $Q_0\Delta t$  over the interval  $[t - \Delta t, t]$  and assumes that the fronts starts at the position reached at the end of the injection in the previous step  $t - \Delta t$ . The second row of sub-figures represents the procedure used by the ILSA scheme assuming

that the front has been moved to the position determined by the prevailing asymptote at the end of the first front iteration.

(i) *Determine equilibrium pressures and widths for the current footprint  $\mathcal{A}$*

Given a trial footprint (initially taken to be that at the previous time step  $\mathcal{A}(t - \Delta t)$  see figure 2 (a)) the coupled equations (3.6) are used to determine the width  $w$  (and hence  $p_f$ ) that corresponds to the fluid flux into the well-bore over the current time step. In the first front iteration (see figure 2 (a)) the crack widths are treated as the primary variable over the whole fracture  $\mathcal{A}$ . In the second and subsequent front iterations, since estimates of the asymptotic tip widths are known (see step (iv) below), the fluid pressures are treated as the primary unknown in the tip region  $\mathcal{A}^t$  and the widths are treated as the primary unknown in the channel region  $\mathcal{A}^c$  (see figure 2 (d));

(ii) *Use tip asymptote to find shortest distances from elements in  $\partial\mathcal{A}^c$  to the new trial crack front  $\mathcal{C}$*

Given the new width estimate  $w$  at each of the survey elements in  $\partial\mathcal{A}^c$  the current trial fracture widths are used to invert the appropriate asymptotic relation from section 2.2.4 to determine the shortest distance  $s$  from the centers of these elements to the free boundary  $\mathcal{C}$ . In particular, (2.9c) can be inverted to obtain  $s$  given  $w_k$ , (2.11) can be inverted to obtain  $s$  given  $w_m$ , (2.12) can be inverted to obtain  $s$  given  $w_{\tilde{m}}$ , the generalized asymptote (2.14) can be inverted to find  $s$  given  $w_{mk}$ , and given  $w_{mk\tilde{m}}$  the generalized asymptote (2.15) can be used to find  $s$ . This process is illustrated in figure 2 (b) and (e) in which the asymptote is represented by the magenta curve, which terminates at the centre of the survey element (just adjacent to the tip element) on the one end and, in the case of this cross section, the other end terminates at the new estimate of the fracture front position.

We observe that all the tip asymptotes (except for the toughness asymptote (2.9c)) involve the unknown front velocity  $V$ , which is so crucial to locating the free boundary. To resolve this issue, if  $s$  is the shortest distance from the current collocation point to the trial free boundary, then in each asymptote involving the front velocity explicitly we replace  $V$  by its difference quotient approximate

$$V = \left( \frac{s - s_{t-\Delta t}}{\Delta t} \right). \quad (3.7)$$

The generalized  $mk$ -asymptote (2.14) has been implemented for plane strain fractures [19] and for planar fractures [33]. For each survey point in  $\partial\mathcal{A}^c$  the trial width  $w$  is used to find  $s$  from the nonlinear equation

$$w_{mk} = \frac{K'^4 \Delta t}{E'^3 \mu' (s - s_{t-\Delta t})} \hat{\Omega} \left( \frac{E'^4 \mu'^2 (s - s_{t-\Delta t})^2 s}{K'^6 \Delta t^2} \right).$$

The generalized  $mk\tilde{m}$ -asymptote (2.15) has been implemented in planar [13] and multi-planar HF models [12]. For each survey point in  $\partial\mathcal{A}^c$  the trial width  $w$  is used to determine  $s$  from

$$\frac{s^2 (s - s_{t-\Delta t}) \mu'}{E' w_{mkc}^3 \Delta t} = g_\delta \left( \frac{K' s^{1/2}}{E' w_{mkc}}, \frac{2C' s^{1/2} \Delta t^{1/2}}{w_{mkc} (s - s_{t-\Delta t})^{1/2}} \right);$$

(iii) *Solve the eikonal equation to locate the new trial crack front  $\mathcal{C}$*

In figure 2 the fracture front is parallel to the sides of the rectangular elements. However, for an arbitrarily shaped fracture boundary this is not the case for all elements of the structured mesh. For this situation, the solution of the eikonal equation is used to reconstruct the front position from the set of shortest distances from the survey elements in  $\partial\mathcal{A}^c$  to the new trial front  $\mathcal{C}$ , which establishes the following initial conditions

$$\mathcal{T}^0(x, y) = -s \text{ for all } (x, y) \in \partial\mathcal{A}^c \quad (3.8)$$

to construct the signed distance function  $\mathcal{T}(x, y)$  by solving the eikonal equation

$$|\nabla \mathcal{T}| = 1. \quad (3.9)$$

The negative sign in the initial condition (3.8) enforces the sign convention that  $\mathcal{T}(x, y) < 0$  for all points  $(x, y)$  that lie within the fracture boundary curve  $\mathcal{C}(t)$ , while points for which  $\mathcal{T}(x, y) > 0$  lie outside  $\mathcal{C}(t)$ . Moreover because the initial condition (3.8) defines the distance to the free boundary, the fracture boundary curve  $\mathcal{C}(t)$  is defined by the level set  $\mathcal{T}(x, y) = 0$ ;

(iv) Set the tip volumes from the asymptote to impose the tip asymptotics in a weak form

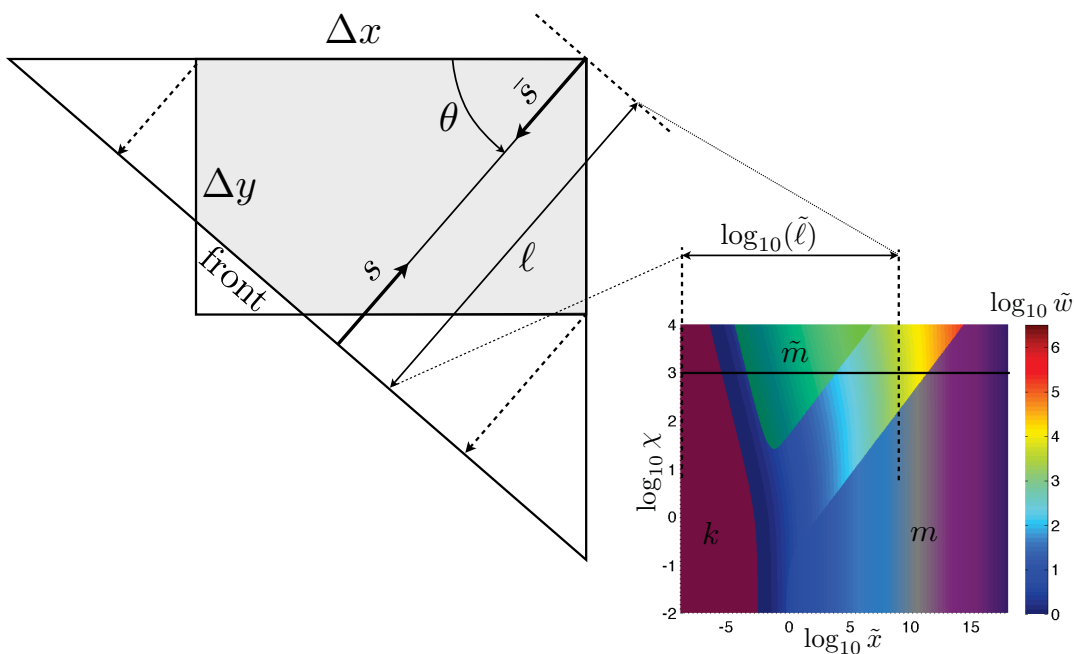


FIGURE 3. Scheme to integrate the asymptotic solution, backwards from the front, over the partially filled rectangular tip element using the integral over a triangle.

Having determined a new estimate for the location of the free boundary  $\mathcal{C}(t)$ , the volume of fluid in each tip element can be determined by integrating the applicable tip asymptote backward from the front to opposite vertex of a triangular region shown in figure 3

$$\mathcal{V}_{\blacktriangle}(\ell) = \frac{2}{\sin 2\theta} \int_0^{\ell} w_a(\ell - \bar{s}) \bar{s} d\bar{s}, \quad (3.10)$$

where  $w_a(s)$  is one of the asymptotes  $w_m$ ,  $w_k$ ,  $w_{\tilde{m}}$ ,  $w_{mk}$ , or  $w_{mk\tilde{m}}$ ,  $\ell$  is the distance from the front to the farthest interior corner of a tip element, and  $\theta$  is the angle that the local outward normal to the front makes with the tip element edge. From the mapping of the span of  $s \in (0, \ell)$  within the element to the interval of length  $\tilde{\ell}$  in the  $\tilde{w}$  map shown in figure 3, we observe that the model is able to capture, in a weak sense, all the multiscale behavior from the computational element scale right down to the finest length scale. The volume over a triangular region  $\mathcal{V}_{\blacktriangle}(\ell)$  can be used to construct the fracture volume within a partially filled rectangular element as follows:

$$\mathcal{V}_{\blacksquare} = \mathcal{V}_{\blacktriangle}(\ell) - \mathcal{V}_{\blacktriangle}(\ell - \Delta x \cos \theta) - \mathcal{V}_{\blacktriangle}(\ell - \Delta y \sin \theta). \quad (3.11)$$

In order to evaluate these integrals only the first two moments of the tip asymptote  $\hat{w}$  are required.

The average width  $w^t$  in the tip element is set to

$$w^t = \frac{\mathcal{V}_{\blacksquare}}{\Delta x \Delta y}.$$

In figure 2 (c) and (f) the asymptotic widths are indicated by the magenta curves while the average tip widths in the tip element are represented by the magenta rectangles.

Since the width in the tip element is determined from the asymptotics once the front position is set, the fluid pressure in the tip element now becomes the primary unknown. The equation for the fluid pressure comes from integrating the Reynolds equation (2.3) over the tip element and applying the zero flux boundary condition. This is precisely the procedure used in the finite volume method and results in an expression for the change in fluid volume over the time step involving  $\mathcal{V}_{\blacksquare}$  that should match the flux of fluid across the boundaries, which involves the fluid pressure at the center of the tip element;

(v) *Convergence check*

If the iterations on the fracture front  $\mathcal{C}$  have converged then proceed to the next time step, if not return to (i) with the new estimate of  $\mathcal{A}$

We observe that the concept of a partially filled element with tip asymptotics imposed in a weak sense is remarkably effective at representing a fracture with an arbitrary front on a structured mesh. The ability to capture the tip asymptotics in a weak form makes it possible to account for multiscale effects that act at length scales that are many orders of magnitude smaller than the computational mesh size. Modeling such multiscale behavior directly would require prohibitively fine meshes. Given that the material parameters are assumed to be fixed, the tip velocity  $V$  is the primary determinant of the region in phase space that a particular asymptote finds itself. Since the ILSA scheme is able to autonomously determine the front velocity  $V$  from the asymptote, it is able to automatically adjust the point in phase space to determine the propagation regime of the fracture front in the neighborhood of the survey points.

In a comparative study [22] this class of schemes was shown to provide accurate solutions on a relatively coarse fixed structured mesh. Recent enhancements to the ILSA strategy [42] have achieved reduced front iterations by using the velocity at the previous step to determine an initial estimate of the front position in the current time step. The ILSA strategy has also been implemented in XFEM HF models [18, 19, 20]. Moreover, since ILSA scheme treats the width as the primary variable in the determination of the fracture front position, it is an ideal candidate to combine with the Extended Kalman Filter to develop a scheme to monitor the evolution of the fracture footprint from remote tiltmeter measurements [36, 32, 26].

## 4 Numerical Results

In this section we present numerical solutions that illustrate the performance of the ILSA strategy for three different examples. In the first two examples we consider a fracture that propagates in an elastic medium in which there are positive jumps in the confining stress field located symmetrically with respect to the fluid source. For the first example we compare the ILSA solution using the  $m$ -vertex solution (2.11) to the results from a laboratory experiment. In the second example we consider the same experimental symmetric stress jump situation, but demonstrate the influence of toughness using the ILSA scheme along with the  $mk$ -asymptote (2.14). In the third example we consider a hydraulic

fracture propagating in a homogeneous elastic medium in which there are jumps in the confining stress field - positive in the layer above and negative in the layer below the fluid source.

#### 4.1 Symmetric stress barrier: $m$ -vertex solution vs experiment and the effect of toughness

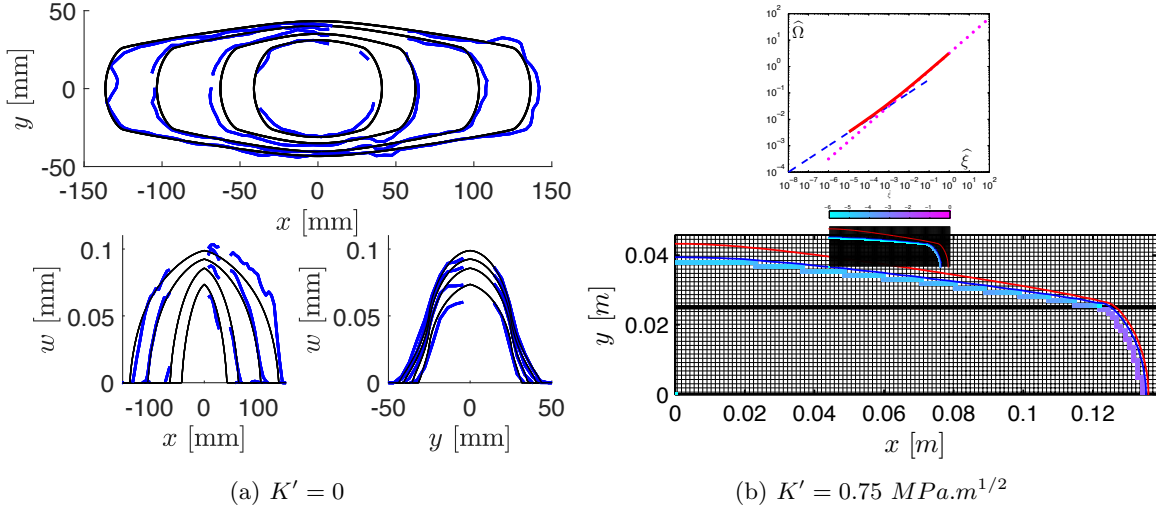


FIGURE 4. Left-Top: Experimental (blue) and ILSA (black) footprints of the blade-shaped fracture formed by a symmetric stress jump in  $\sigma_0$  at times  $t = 88, 171, 375, 603$  s; Left-Bottom: Experimental (blue) and ILSA (black) fracture widths (left cross section  $y = 0$ ) and (right cross section  $x = 0$ ) at the same time steps; Right: Fracture footprint  $C(t)$  at time  $t = 600$  s for  $K' = 0.75 \text{ MPa.m}^{1/2}$ . The M-vertex footprint (shown red online) encompasses the MK footprint (shown blue online), which is sampled at the corresponding time.

In this section we compare the ILSA  $m$ -vertex solution with the results of a laboratory experiment [21] in which an HF was initiated at the center of a layer of height  $H = 50 \text{ mm}$  bounded symmetric stress jumps  $\Delta\sigma = 4.3 \text{ MPa}$  in  $\sigma_0$ , which is given by

$$\sigma_0 = \begin{cases} 2.2 \text{ MPa} & \text{for } |y| < 25 \text{ mm} \\ 6.5 \text{ MPa} & \text{for } |y| > 25 \text{ mm}. \end{cases}$$

The ILSA model uses the following parameter values reported for the experiment:

$$E = 3.3 \text{ MPa}, \nu = 0.4, \mu = 30.2 \text{ Pa.s}, K' = 0, C' = 0, Q_0 = 0.0017 \text{ ml/s}$$

Since the fracture takes place between two un-bonded impermeable blocks of PMMA, the fracture in the experiment propagates in the  $m$ -vertex viscous regime. In figure 4 (a) the experimental (blue) and ILSA (black) blade-like fracture footprints and fracture width cross-sections with the planes  $y = 0$  and  $x = 0$  are compared at a sequence of sample times. The numerical results show remarkable agreement with the experimental results. In figure 4 (b) we compare the ILSA results using the  $m$ -vertex and  $mk$ -asymptote  $K' = 0.75 \text{ MPa.m}^{1/2}$  at  $t = 600$ s, while all the other parameters are kept the same. In this plot the DD mesh is denoted by the thin grid lines and the thick horizontal lines represent the interface across which the confining stress field jumps. The colored survey elements indicate the different length scale active at each point of the fracture boundary, which corresponds to color bar located below the  $\hat{\xi}$  axis in the plot of the generalized asymptote  $\hat{\Omega}$  vs  $\hat{\xi}$ .

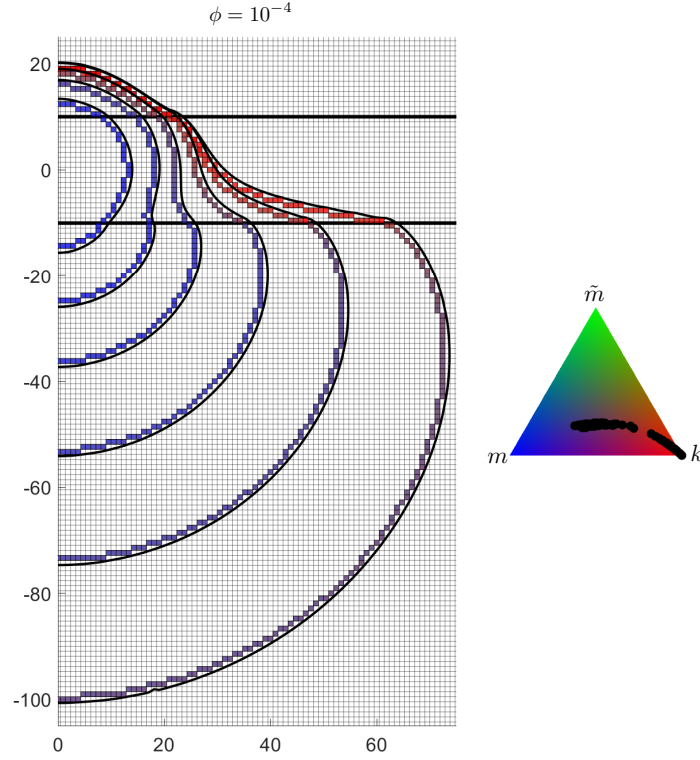


FIGURE 5. Hydraulic fracture footprints calculated for the stress drop geometry defined in (4.1) for  $\phi = 10^{-4}$  at the time instants  $t = \{112.5, 225, 450, 900, 1800, 3600\}$  s.

#### 4.2 A stress drop: distinct propagation regimes along the periphery

In this section we illustrate the ILSA solution using the generalized  $mkc$ -asymptote (2.15) for a hydraulic fracture propagating in a confining stress field  $\sigma_0$  that drops discontinuously across two interfaces a distance  $H = 20$  m apart. The material parameters used in this example are

$$E = 9.5 \text{ GPa}, \nu = 0.2, \mu = 0.1 \text{ Pa}\cdot\text{s}, K' = 3.192 \text{ MPa}\cdot\text{m}^{1/2}, C' = 0.521 \times 10^{-5} \text{ m/s}^{1/2}, Q_0 = 0.01 \text{ m}^3/\text{s},$$

while the confining stress field is defined by

$$\sigma_0 = \begin{cases} 7.25 \text{ MPa} & \text{for } y > 10 \text{ m} \\ 7 \text{ MPa} & \text{for } |y| < 10 \text{ m} \\ 6.5 \text{ MPa} & \text{for } y < -10 \text{ m} \end{cases} \quad (4.1)$$

The dimensionless leak-off parameter [24] associated with this parameter set is given by  $\phi = \frac{\mu'^3 E'^{11} C'^4 Q_0}{K'^{14}} = 10^{-4}$ . The survey elements are colored according to the location of the corresponding asymptotic solution in the parametric  $mkc$ -triangle. Black circular markers inside the parametric triangle shows the positions of all survey elements for the footprint that corresponds to the last time instant  $t = 3600$  s.

## 5 Conclusions

In this chapter we have described how to build efficient numerical schemes to model HF propagation that exploit the recent advancements the analysis of the multiscale tip asymptotic behavior that occurs on multiple time scales as the different physical processes of viscous dissipation, energy required to break the rock associated with toughness, and

diffusive leak-off of fluid into the porous rock. As a starting point we briefly summarized the governing equations, boundary and propagation conditions, and the limiting tip asymptotic behavior needed in the construction of these algorithms. We then illustrate in detail the process of iterative location of the free boundary and capture, in a weak sense, of the multiscale behavior relevant at the computational scale by the integration of the tip asymptote down to the finest scale active in the problem. We conclude by providing some numerical results illustrating the performance of the algorithm for the following problems: viscosity dominated propagation compared with experiments; two-process (viscous-toughness) propagation in a symmetric stress

### Acknowledgements

The author gratefully acknowledges grant support from NSERC (Canada) and the BC Oil and Gas Commission.

### References

- [1] Adachi J.I. and Detournay E., Plane-strain propagation of a fluid-driven fracture in a permeable medium, *Engrg. Fract. Mech.* 75,4666-4694, 2008.
- [2] Adachi, J., Siebrits, E., Peirce, A. and Desroches, J. Computer Simulation of Hydraulic Fractures. *International Journal of Rock Mechanics & Mining Systems* 44(5),p. 739-757, 2007.
- [3] Bungler A.P., Detournay E. Experimental validation of the tip asymptotics for a fluid-driven crack. *J. Mech. Phys. Solids* 56:310115, 2008.
- [4] Carter, E.D. Optimum fluid characteristics for fracture extension, in: G.C. Howard, C.R. Fast (Eds.), *Drilling and Production Practices*, American Petroleum Institute, Tulsa, OK, 1957, pp. 261-270.
- [5] Clifton R.J., Abou-Sayed A.S. 1979. On the computation of the three-dimensional geometry of hydraulic fractures. *Proc. 1979 SPE Symp. Low Permeability Gas Reserv.*, SPE 7943. Richardson TX: Soc. Petrol. Eng.
- [6] Crouch, S.L. and Starfield, A.M., *Boundary Element Methods in Solid Mechanics*, George Allen and Unwin, London, 1983.
- [7] Desroches, J., Detournay, E., Lenoach, B., Papanastasiou, P., Pearson, J.R.A., Thiercelin, M., and Cheng, A.H.D., *The Crack Tip Region in Hydraulic Fracturing*, *Proc. R. Soc. London, Ser. A*, 447, pp. 394-408, 1994.
- [8] Detournay E., *Mechanics of Hydraulic Fractures*, *Annu. Rev. Fluid Mech.* 48:311-339, 2016.
- [9] Detournay E. and Peirce A., *On the Moving Boundary Conditions for a Hydraulic Fracture*, *Int. J. Eng. Sci.*, (accepted for publication 22 December 2013).
- [10] Dontsov, E., Peirce, A., An enhanced pseudo-3D model for hydraulic fracturing accounting for viscous height growth, non-local elasticity, and lateral toughness, *Engineering Fracture Mechanics*, 42, p 116-139, 2015.
- [11] Dontsov, E., Peirce, A., A non-singular integral equation formulation to analyse multiscale behaviour in semi-infinite hydraulic fractures, *J. Fluid Mech (JFM RAPIDS)*, vol. 781, R1, 2015.
- [12] Dontsov, E., Peirce, A., Implementing a universal tip asymptotic solution into an Implicit Level Set Algorithm (ILSA) for multiple parallel hydraulic fractures, Submitted to *Proceedings of Amer. Rock Mech. Assoc. (ARMA2016) Houston*, ARMA 16-268, 2016.
- [13] Dontsov, E., Peirce, A., A multiscale Implicit Level Set Algorithm (ILSA) to model hydraulic fracture propagation incorporating combined viscous, toughness, and leak-off asymptotics, *Comp. Meth. in Appl. Mech. and Eng.*, 313, 53-84, 2017.
- [14] Economides, M.J. and K.G. Nolte (editors), *Reservoir Stimulation*, John Wiley & Sons, Ltd., New York, 2000.
- [15] Garagash D., *Near-Tip Processes of Fluid-Driven Fractures*, Ph.D. thesis, University of Minnesota, Minneapolis, 1998.
- [16] Garagash D.I. and Detournay E., The tip region of a fluid-driven fracture in an elastic medium, *ASME J. Appl. Mech.*, 67, (1) pp 183-192, 2000.
- [17] Garagash, D., E. Detournay, and J. Adachi, multi-scale tip asymptotics in hydraulic fracture with leak-off. *J. Fluid Mech.*, 669, 260-297, 2011.
- [18] Gordeliy, E. and Peirce, A. P., Coupling schemes for modeling hydraulic fracture propagation using the XFEM, *Comp. Meth. in Appl. Mech. and Eng.*, 253, p305-322, 2013.
- [19] Gordeliy, E. and Peirce, A. P., Implicit level set schemes for modeling hydraulic fractures using the XFEM, *Comp. Meth. in Appl. Mech. and Eng.*, 266, p125-143, 2013.
- [20] Gordeliy, E. and Peirce, A. P., Enrichment strategies and convergence properties of the XFEM for hydraulic fracture problems, *Comp. Meth. in Appl. Mech. and Eng.*, 283, p474-502, 2015.

- [21] Jeffrey, R.G. and Bunger, A.P., A Detailed Comparison of Experimental and Numerical Data on Hydraulic Fracture Height Growth through Stress Contrasts. *SPE Journal*, 14(3):413-422, 2009.
- [22] Lecampion B., Peirce A.P, Detournay E., Zhang X., Chen Z., Bunger A.P., Detournay C., Napier J., Abbas S., Garagash D., Cundall, P., The impact of the Near-Tip Logic on the Accuracy and Convergence Rate of Hydraulic Fracture Simulators Compared to Reference solutions. In: *Effective and Sustainable Hydraulic Fracturing*, AP Bunger, J McLennan and R Jeffrey (eds.), ISBN 978-953-51-1137-5, (Intech), Chapter 43, p 855-873, 2013.
- [23] Lenoach B. The crack tip solution for hydraulic fracturing in a permeable solid. *J. Mech. Phys. Solids* 43:1025-43, 1995.
- [24] Madyarova, M., Fluid-Driven Penny-Shaped Fracture in Permeable Rock, Ph.D. Thesis, University of Minnesota, 2003.
- [25] Oberhettinger, F., *Tables of Mellin transforms*, Springer-Verlag, NY, 1970.
- [26] Pandurangan, V., Peirce, A., Chen, Z.R. and Jeffrey, R.G., "Tiltmeter Mapping of Asymmetric Hydraulic Fracture Growth using the Implicit Level Set Algorithm and the Extended Kalman filter" submitted to *Inverse Problems*.
- [27] Peirce, A., Spottiswoode, S. & Napier, J.A.L. The spectral boundary element method: A new window on boundary elements in rock mechanics, *Int. J. of Rock Mech. and Min. Sci. & Geomech. Abstr.*, Vol. 29, No. 4, pp. 379-400, 1992.
- [28] Peirce, A. & Napier, J.A.L., "A spectral multipole method for efficient solution of large-scale boundary element models in elastostatics", *Int. J. Num. Meth. Eng.*, Vol. 38, pp. 4009-4034, 1995.
- [29] Peirce, A.P. and Siebrits, E., A dual mesh Multigrid preconditioner for the efficient solution of hydraulically driven fracture problems, *Int. J. for Num. Meth. Eng.*, 63, 13, 1797-1823, 2005.
- [30] Peirce, A., Localized Jacobain ILU Preconditioners for Hydraulic Fractures, *Int. J. for Num. Meth. Eng.*, 65, 12, 1935-1946, 2006.
- [31] Peirce, A. and Detournay, E. An Implicit Level Set Method for Modeling Hydraulically Driven Fractures. *Computer Methods and Applied Mechanics*, 197, 2858-2885, 2008.
- [32] Peirce, A. and Rochinha F., An Integrated Extended Kalman Filter Implicit Level Set Algorithm for monitoring Planar Hydraulic Fracture, *Inverse Problems*, 28, 2012.
- [33] Peirce, A., Modeling multi-scale processes in hydraulic fracture propagation using the implicit level set algorithm, *Comp. Meth. in Appl. Mech. and Eng.*, 283, p 881-908, 2015.
- [34] A.P. Peirce, Implicit level set algorithms for modelling hydraulic fracture propagation, *Phil. Trans. R. Soc. A* 374 (2016) 20150423.
- [35] Rice, J. R., *Mathematical Analysis in the Mechanics of Fracture, Fracture, an Advanced Treatise*, H. Liebowitz, ed. Academic Press, New York, Chap. 3, pp. 191-311, 1968.
- [36] Rochinha, F. and Peirce, A., Monitoring Hydraulic Fractures: State Estimation using an Extended Kalman Filter, *Inverse Problems*, 26, 2, 025009, 17p, 2010.
- [37] Sethian, J.A., *Level Set Methods and Fast Marching Methods: Evolving Interfaces in Computational Geometry Fluid Mechanics Computer Vision and Materials Science*, Cambridge University Press, Cambridge, UK, 1999.
- [38] Spence, D.A. and Sharp, P., Self-Similar Solutions for Elastohydro Dynamic Cavity Flow, *Proc.R.Soc.London, Ser.A*, 400, pp.289313, 1985.
- [39] Spence D.A. and Sharp P.W., and Turcotte D.L., Buoyancy-driven crack propagation: a mechanism for magma migration, *J. Fluid Mech.* 174, pp. 135-153, 1987.
- [40] Siebrits, E. and Peirce, A.P., An efficient multi-layer planar 3D fracture growth algorithm using a fixed mesh approach, *Int. J. Numer. Methods Engrg.* 53, pp 691717, 2002.
- [41] van As, A. and Jeffrey R.G., Caving induced by hydraulic fracturing at North Parkes mines, in: *Pacific Rocks 2000*, Balkema, Rotterdam, 2000, pp.353-360.
- [42] Zia, H. and Lecampion, B. (2019). Explicit versus implicit front advancing schemes for the simulation of hydraulic fracture growth. *Int. J. Numer. Anal. Meth. Geomech.*, 43(6):13001315.